DAMA/LIBRA-phase2 in WIMP effective models

Sunghyun Kang, Stefano Scopel, Gaurav Tomar, Jong-Hyun Yoon

Department of Physics, Sogang University, Seoul, Korea, 121-742

E-mail: scopel@sogang.ac.kr, tomar@sogang.ac.kr, francis735@naver.com, jyoon@sogang.ac.kr

Abstract. The DAMA/LIBRA collaboration has recently released updated results from their search for the annual modulation signal expected from Dark Matter (DM) scattering in their NaI detectors. We have fitted the updated DAMA result for the modulation amplitudes in terms of a Weakly Interacting Massive Particle (WIMP) signal, parameterizing the interaction with nuclei in terms of the most general effective Lagrangian for a WIMP particle spin up to 1/2, systematically assuming dominance of one of the 14 possible interaction terms, and assuming for the WIMP velocity distribution a standard Maxwellian. We find that most of the couplings of the non–relativistic effective Hamiltonian can provide a better fit compared to the standard Spin Independent interaction case, and with a reduced fine–tuning of the three parameters (WIMP mass, WIMP–nucleon effective cross-section and ratio between the WIMP–neutron and the WIMP–proton couplings). Moreover, effective models for which the cross section depends explicitly on the WIMP incoming velocity can provide a better fit of the DAMA data at large values of m_χ compared to the standard velocity–independent cross–section due to a different phase of the modulation amplitudes. All the best fit solutions are in tension with exclusion plots of both XENON1T and PICO60.

C	ontents	
1	Introduction	1
2	WIMP rates in non–relativistic effective models	3
3	Analysis	6
4	Conclusions	12
\mathbf{A}	WIMP response functions	15
В	Constraints	15
	B.1 XENON1T	15
	B.2 PICO60	16

1 Introduction

Weakly Interacting Massive Particles (WIMPs) are the most popular candidates to provide the Dark Matter (DM) which is believed to make up 27% of the total mass density of the Universe [1] and more than 90% of the halo of our Galaxy, and a worldwide experimental effort is under way to detect them. In particular the DAMA experiment [2–4] has been measuring for more than 15 years a yearly modulation effect with a sodium iodide target consistent with that expected due to the Earth rotation around the Sun from the elastic scattering of WIMPs, claiming a statistical significance of more than 9 σ . Many experimental collaborations using nuclear targets different from NaI and various background–subtraction techniques to look for WIMP–elastic scattering (XENON1T [5], LUX [6], XENON100 [7], XENON10 [8], KIMS [9, 10], CDMS-Ge [11], CDMSlite [12], SuperCDMS [13], CDMS II [14], SIMPLE [15], COUPP [16], PICASSO [17], PICO-2L [18], PICO-60 [19]) have failed to observe any anomaly so far, implying severe constraints on the most popular WIMP scenarios used to explain the DAMA excess.

Recently the DAMA collaboration has released first result from the upgraded DAMA/LIBRA-phase2 experiment [20]. The two most important improvements compared to the previous data is that now the exposure has almost doubled and the energy threshold has been lowered from 2 keV electron–equivalent (keVee) to 1 keVee. In particular, this latter feature has improved the chances to exploit the DAMA annual modulation amplitudes spectral energy shape to test specific WIMP models. The most popular of them, predicted in ultraviolet completions of the Standard Model such as Supersymmetry or Large Extra Dimensions, implies a Spin–Independent (SI) WIMP–nucleus scattering cross section $\sigma_{\chi N}$ that scales with the square of the number of nucleon targets in the nucleus:

$$\sigma_{\chi N} \propto \left[c^p Z + (A - Z)c^n\right]^2,\tag{1.1}$$

with A the nuclear mass number, Z the nuclear charge and $c^{p,n}$ the WIMP couplings to protons and neutrons, with $c^n=c^p$ (i.e. an isoscalar interaction) in the most natural realizations. On the other hand, the expected WIMP-induced scattering spectrum depends on a convolution on the velocity distribution $f(\vec{v})$ of the incoming WIMPs, usually described by a

thermalized non-relativistic gas described by a Maxwellian distribution whose r.m.s. velocity $v_{rms} \simeq 270 \text{ km/s}$ is determined from the galactic rotational velocity by assuming equilibrium between gravitational attraction and WIMP pressure. Indeed, such model, usually referred to as Isothermal Sphere, is confirmed by numerical simulations[21], although the detailed merger history of the Milky Way is not known, allowing for the possibility of the presence of sizable non-thermal components for which the density, direction and speed of WIMPs are hard to predict[22].

The combination of a SI isoscalar cross section with the Isothermal Sphere model has provided for a long time a good fit to the DAMA results in Refs.[2–4], either for a light WIMP mass, $m_\chi \simeq 10$ GeV [23, 24], or for a heavy WIMP mass $m_\chi \lesssim 100$ GeV. However, as pointed out in Refs.[25] and [26], with the new DAMA data the goodness of fit of such scenario has considerably worsened, and is now disfavored (at 5.1 σ for the low-mass solution, $m_\chi \simeq 8$ GeV and at 3.2 σ for the high mass solution, $m_\chi \simeq 53$ GeV [25]). On the other hand an acceptable fit can be obtained by allowing for a substantial isovector component in the WIMP–nucleon interaction, although at the price of tuning the coupling ratio in order to suppress the WIMP-iodine interaction.

Although theoretically motivated, a SI WIMP–nucleus cross section is not the only possible WIMP–nucleus interaction. Actually, the non-observation so far of new physics at the Large Hadron Collider has strongly prompted for the necessity to go beyond this "top-down" approach in order to extend the search of Dark Matter candidates to a wider range of properties through an alternative "bottom-up" strategy not biased by theoretical prejudice. In particular the WIMP–nucleus cross section can be parameterized in terms of the most general non–relativistic effective theory complying with Galilean symmetry, including a possible explicit dependence of $\sigma_{\chi N}$ on the transferred momentum and on the WIMP incoming velocity [27–30].

Also within such effective framework it has been shown that a strong tension persists between an interpretation of the DAMA modulation effect in terms of a WIMP signal and the results of null experiments [31], if a Maxwellian velocity distribution for the WIMPs is assumed. Nevertheless no fit of the DAMA result is available in the literature in terms of non-relativistic EFT models. Moreover, in addition to increasing the exposure, the phase 2 result also includes a lower energy threshold, and the new spectrum of modulation amplitudes no longer shows a maximum, but is rather monotonically decreasing with energy. In light of these differences it is significant to extend an assessment of the goodness of fit of the new DAMA result to such scenarios. To this aim, and making the same assumptions on the WIMP velocity distribution, in the present paper we wish to discuss how effective WIMP-nucleus interactions can fit the new DAMA data. On top of that, in the analysis of Ref. [31] it was shown that a combination of xenon and fluorine targets (namely XENON1T and PICO60) was needed to exclude all the effective theory parameter space. Such assessment made only use of the size of the modulation amplitudes in the first three bins of the experimental result in Refs. [2-4], but did not exploit the goodness of fit information. So in the present paper we will also compare the best-fit parameter space of a WIMP interpretation of the DAMA result to the present constraints from XENON1T and PICO60.

In our approach we will consider the most general WIMP–nucleus effective Lagrangian for a WIMP particle of spin 0 or spin 1/2 scattering elastically off nuclei, systematically assuming the dominance of one of the 14 possible interaction terms of the most general non–relativistic Hamiltonian invariant by Galilean transformations [29, 30], fitting the new DAMA data to the three parameters m_{χ} (WIMP mass), σ_p (WIMP–nucleon effective cross-

section) and c^n/c^p . Specifically, the goals of our analysis are i) to check if a fit to the DAMA data better than in the standard SI case can be obtained by using any of the non-standard interactions of the non-relativistic effective theory; ii) if this is possible with less fine-tuning of the parameters (in particular of the ratio c^n/c^p) compared to the SI case; iii) to check in each case the level of tension between a DAMA interpretation in terms of a WIMP annual modulation signal and the null results from other experiments (in the following we will consider the two representative bounds from XENON1T and PICO60).

The paper is organized as follows. In Section 2 we summarize the non–relativistic Effective Field Theory (EFT) approach of Ref.[29, 30] and provide the formulas to calculate expected rates for WIMP–nucleus scattering; in Section 3 we analyze the DAMA result including the latest upgrade by comparing the measured modulation amplitudes to the calculated ones in a chi square analysis where in a systematic way each of the couplings of the effective non–relativistic Hamiltonian is assumed to be the dominant one. We will provide our conclusions in Section 4. In Appendix A we provide for completeness the WIMP response functions for the non–relativistic effective theory while in Appendix B we provide the details of the calculations of the constraints from XENON1T and PICO60.

2 WIMP rates in non-relativistic effective models

Making use of the non-relativistic EFT approach of Ref. [29, 30] the most general Hamiltonian density describing the WIMP-nucleus interaction can be written as:

$$\mathcal{H}(\mathbf{r}) = \sum_{\tau=0,1} \sum_{j=1}^{15} c_j^{\tau} \mathcal{O}_j(\mathbf{r}) t^{\tau}, \qquad (2.1)$$

where:

$$\mathcal{O}_{1} = 1_{\chi} 1_{N}; \quad \mathcal{O}_{2} = (v^{\perp})^{2}; \quad \mathcal{O}_{3} = i\vec{S}_{N} \cdot (\frac{\vec{q}}{m_{N}} \times \vec{v}^{\perp})
\mathcal{O}_{4} = \vec{S}_{\chi} \cdot \vec{S}_{N}; \quad \mathcal{O}_{5} = i\vec{S}_{\chi} \cdot (\frac{\vec{q}}{m_{N}} \times \vec{v}^{\perp}); \quad \mathcal{O}_{6} = (\vec{S}_{\chi} \cdot \frac{\vec{q}}{m_{N}})(\vec{S}_{N} \cdot \frac{\vec{q}}{m_{N}})
\mathcal{O}_{7} = \vec{S}_{N} \cdot \vec{v}^{\perp}; \quad \mathcal{O}_{8} = \vec{S}_{\chi} \cdot \vec{v}^{\perp}; \quad \mathcal{O}_{9} = i\vec{S}_{\chi} \cdot (\vec{S}_{N} \times \frac{\vec{q}}{m_{N}})
\mathcal{O}_{10} = i\vec{S}_{N} \cdot \frac{\vec{q}}{m_{N}}; \quad \mathcal{O}_{11} = i\vec{S}_{\chi} \cdot \frac{\vec{q}}{m_{N}}; \quad \mathcal{O}_{12} = \vec{S}_{\chi} \cdot (\vec{S}_{N} \times \vec{v}^{\perp})
\mathcal{O}_{13} = i(\vec{S}_{\chi} \cdot \vec{v}^{\perp})(\vec{S}_{N} \cdot \frac{\vec{q}}{m_{N}}); \quad \mathcal{O}_{14} = i(\vec{S}_{\chi} \cdot \frac{\vec{q}}{m_{N}})(\vec{S}_{N} \cdot \vec{v}^{\perp})
\mathcal{O}_{15} = -(\vec{S}_{\chi} \cdot \frac{\vec{q}}{m_{N}})((\vec{S}_{N} \times \vec{v}^{\perp}) \cdot \frac{\vec{q}}{m_{N}}), \tag{2.2}$$

In the above equation $1_{\chi N}$ is the identity operator, \vec{q} is the transferred momentum, \vec{S}_{χ} and \vec{S}_{N} are the WIMP and nucleon spins, respectively, while $\vec{v}^{\perp} = \vec{v} + \frac{\vec{q}}{2\mu_{\chi N}}$ (with $\mu_{\chi N}$ the WIMP-nucleon reduced mass) is the relative transverse velocity operator satisfying $\vec{v}^{\perp} \cdot \vec{q} = 0$. For a nuclear target T it can also be written as:

$$(v_T^{\perp})^2 = v_T^2 - v_{min}^2. (2.3)$$

where, for WIMP-nucleus elastic scattering:

$$v_{min}^2 = \frac{q^2}{4\mu_T^2} = \frac{m_T E_R}{2\mu_T^2},\tag{2.4}$$

represents the minimal incoming WIMP speed required to impart the nuclear recoil energy E_R , while $v_T \equiv |\vec{v}_T|$ is the WIMP speed in the reference frame of the nuclear center of mass, m_T the nuclear mass and μ_T the WIMP-nucleus reduced mass. Moreover $t^0=1$, $t^1=\tau_3$ denote the the 2×2 identity and third Pauli matrix in isospin space, respectively, and the isoscalar and isovector (dimension -2) coupling constants c_j^0 and c_j^1 , are related to those to protons and neutrons c_j^p and c_j^n by $c_j^p=(c_j^0+c_j^1)/2$ and $c_j^n=(c_j^0-c_j^1)/2$. Operator \mathcal{O}_2 is of higher order in v compared to all the others, implying a cross section

Operator \mathcal{O}_2 is of higher order in v compared to all the others, implying a cross section suppression of order $\mathcal{O}(v/c)^4) \simeq 10^{-12}$ for the non-relativistic WIMPS in the halo of our Galaxy. Moreover it cannot be obtained from the leading-order non relativistic reduction of a manifestly relativistic operator [29]. So, following Ref.[29, 30], we will not include it in our analysis.

Assuming that the nuclear interaction is the sum of the interactions of the WIMPs with the individual nucleons in the nucleus the WIMP scattering amplitude on the target nucleus T can be written in the compact form:

$$\frac{1}{2j_{\chi}+1}\frac{1}{2j_{T}+1}|\mathcal{M}|^{2} = \frac{4\pi}{2j_{T}+1}\sum_{\tau=0,1}\sum_{\tau'=0,1}\sum_{k}R_{k}^{\tau\tau'}\left[c_{j}^{\tau},(v_{T}^{\perp})^{2},\frac{q^{2}}{m_{N}^{2}}\right]W_{Tk}^{\tau\tau'}(y). \tag{2.5}$$

In the above expression j_{χ} and j_{T} are the WIMP and the target nucleus spins, respectively, $q=|\vec{q}|$ while the $R_{k}^{\tau\tau'}$'s are WIMP response functions (that we report for completeness in Eq.(A.1)) which depend on the couplings c_{j}^{τ} as well as the transferred momentum \vec{q} and $(v_{T}^{\perp})^{2}$. In equation (2.5) the $W_{Tk}^{\tau\tau'}(y)$'s are nuclear response functions and the index k represents different effective nuclear operators, which, crucially, under the assumption that the nuclear ground state is an approximate eigenstate of P and CP, can be at most eight: following the notation in [29, 30], k=M, Φ'' , $\Phi''M$, $\tilde{\Phi}'$, Σ'' , Σ' , $\Delta,\Delta\Sigma'$. The $W_{Tk}^{\tau\tau'}(y)$'s are function of $y \equiv (qb/2)^{2}$, where b is the size of the nucleus. For the target nuclei T used in most direct detection experiments the functions $W_{Tk}^{\tau\tau'}(y)$, calculated using nuclear shell models, have been provided in Refs.[30, 32].

For a given recoil energy imparted to the target the differential rate for the WIMP–nucleus scattering process is given by:

$$\frac{dR_{\chi T}}{dE_R}(t) = \sum_T N_T \frac{\rho_{\text{WIMP}}}{m_{\text{WIMP}}} \int_{v_{min}} d^3 v_T f(\vec{v}_T, t) v_T \frac{d\sigma_T}{dE_R}, \tag{2.6}$$

where ρ_{WIMP} is the local WIMP mass density in the neighborhood of the Sun, N_T the number of the nuclear targets of species T in the detector (the sum over T applies in the case of more than one target), while

$$\frac{d\sigma_T}{dE_R} = \frac{2m_T}{4\pi v_T^2} \left[\frac{1}{2j_X + 1} \frac{1}{2j_T + 1} |\mathcal{M}_T|^2 \right],\tag{2.7}$$

with the squared amplitude in parenthesis given explicitly in Eq.(2.5). Finally, $f(\vec{v}_T)$ is the WIMP velocity distribution, for which we assume a standard isotropic Maxwellian at rest in

the Galactic rest frame truncated at the escape velocity u_{esc} , and boosted to the Lab frame by the velocity of the Earth. So for the former we assume:

$$f(\vec{v}_T, t) = \frac{1}{N} \left(\frac{3}{2\pi v_{rms}^2} \right)^{3/2} e^{-\frac{3|\vec{v}_T + \vec{v}_E|^2}{2v_{rms}^2}} \Theta(u_{esc} - |\vec{v}_T + \vec{v}_E(t)|)$$
 (2.8)

$$N = \left[\text{erf}(z) - \frac{2}{\sqrt{\pi}} z e^{-z^2} \right]^{-1}, \tag{2.9}$$

with $z = 3u_{esc}^2/(2v_{rms}^2)$. In the isothermal sphere model hydrothermal equilibrium between the WIMP gas pressure and gravity is assumed, leading to $v_{rms} = \sqrt{3/2}v_0$ with v_0 the galactic rotational velocity. The yearly modulation effect is due to the time dependence of the Earth's speed with respect to the Galactic frame:

$$\vec{v}_E(t) = v_{Sun} + v_{orb}\cos\gamma\cos\left[\frac{2\pi}{T_0}(t - t_0)\right],\tag{2.10}$$

where $\cos \gamma \simeq 0.49$ accounts for the inclination of the ecliptic plane with respect to the Galactic plane, $T_0=1$ year, $t_0=2$ June, $v_{orb}=2\pi r_{\oplus}/(T_0)\simeq 29$ km/s ($r_{\oplus}=1$ AU, neglecting the small eccentricity of the Earth's orbit around the Sun) while $v_{Sun}=v_0+12$, accounting for a peculiar component of the solar system with respect to the galactic rotation. For the two parameters v_0 and u_{esc} we take $v_0=220$ km/s [33] and $u_{esc}=550$ km/s [34]. In the isothermal model the time dependence of Eq. (2.10) induces an expected rate with the functional form $S(t)=S_0+S_m\cos(2\pi/T-t_0)$, with $S_m>0$ at large values of v_{min} and turning negative when $v_{min}\lesssim 200$ km/s. In such regime of v_{min} and below the phase is modified by the focusing effect of the Sun's gravitational potential [35], while when $S_m\ll S_0$ the time dependence differs from a simple cosine due the contribution of higher harmonics[36].

The expected rate in a given visible energy bin $E_1' \leq E' \leq E_2'$ of a direct detection experiment is given by:

$$R_{[E'_1, E'_2]}(t) = MT_{exp} \int_{E'_1}^{E'_2} \frac{dR}{dE'}(t) dE'$$
(2.11)

$$\frac{dR}{dE'}(t) = \sum_{T} \int_{0}^{\infty} \frac{dR_{\chi T}(t)}{dE_{ee}} \mathcal{G}_{T}(E', E_{ee}) \epsilon(E') dE_{ee}$$
 (2.12)

$$E_{ee} = q(E_R)E_R, (2.13)$$

with $\epsilon(E') \leq 1$ the experimental efficiency/acceptance. In the equations above E_R is the recoil energy deposited in the scattering process (indicated in keVnr), while E_{ee} (indicated in keVee) is the fraction of E_R that goes into the experimentally detected process (ionization, scintillation, heat) and $q(E_R)$ is the quenching factor, $\mathcal{G}_T(E', E_{ee} = q(E_R)E_R)$ is the probability that the visible energy E' is detected when a WIMP has scattered off an isotope T in the detector target with recoil energy E_R , M is the fiducial mass of the detector and T_{exp} the live—time exposure of the data taking.

In particular, in each visible energy bin DAMA is sensitive to the yearly modulation amplitude S_m , defined as the cosine transform of $R_{[E'_1,E'_2]}(t)$:

$$S_{m,[E'_1,E'_2]} \equiv \frac{2}{T_0} \int_0^{T_0} \cos\left[\frac{2\pi}{T_0}(t-t_0)\right] R_{[E'_1,E'_2]}(t)dt, \tag{2.14}$$

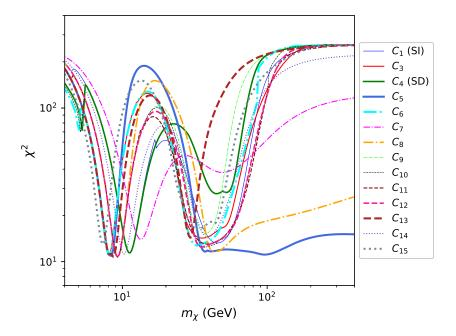


Figure 1. Minimum of the χ^2 of Eq.(3.1) at fixed WIMP mass m_{χ} as a function of m_{χ} for different WIMP-nucleus interactions.

while other experiments put upper bounds on the time average S_0 :

$$S_{0,[E'_1,E'_2]} \equiv \frac{1}{T_0} \int_0^{T_0} R_{[E'_1,E'_2]}(t)dt.$$
 (2.15)

In the present paper we will systematically consider the possibility that one of the couplings c_j dominates in the effective Hamiltonian of Eq. (2.1). In this case it is possible to factorize a term $|c_j^p|^2$ from the squared amplitude of Eq.(2.5) and express it in terms of the effective WIMP-proton cross section:

$$\sigma_p = (c_j^p)^2 \frac{\mu_{\chi \mathcal{N}}^2}{\pi},\tag{2.16}$$

(with $\mu_{\chi\mathcal{N}}$ the WIMP-nucleon reduced mass) and the ratio $r \equiv c_j^n/c_j^p$. It is worth pointing out here that among the generalized nuclear response functions arising from the effective Hamiltonian (2.1) only the ones corresponding to M (SI interaction), Σ'' and Σ' (both related to the standard spin-dependent interaction) do not vanish for $q \to 0$, and so allow to interpret σ_p in terms of a long-distance, point-like cross section. In the case of the other interactions Φ'' , $\Phi''M$, $\tilde{\Phi}'$, Δ and $\Delta\Sigma'$ the quantity σ_p is just a convenient alternative to directly parameterizing the interaction in terms of the c_j^p coupling.

3 Analysis

The DAMA collaboration has recently released modulation amplitudes $S_{m,k}^{exp} \equiv S_{m,[E'_k,E'_{k+1}]}$, with uncertainties σ_k , (corresponding to the predictions of Eq.(2.14)) in the visible energy

$\mathbf{c_{j}}$	$ m m_{\chi,min}~(GeV)$	$\mathbf{r}_{\chi,\mathbf{min}}$	$\sigma \ (\mathrm{cm^2})$	χ^2_{\min}
	11.17	-0.76	2.67e-38	11.38
c_1	45.19	-0.66	1.60e-39	13.22
	8.10	-3.14	2.27e-31	11.1
c_3	35.68	-1.10	9.27e-35	14.23
a.	11.22	1.71	2.95e-36	11.38
c_4	44.71	-8.34	5.96e-36	27.7
0-	8.34	-0.61	1.62e-29	10.83
c_5	96.13	-5.74	3.63e-34	11.11
0-	8.09	-7.20	5.05e-28	11.11
c_6	32.9	-6.48	5.18e-31	12.74
<i>c</i> -	13.41	-4.32	4.75e-30	13.94
C7	49.24	-0.65	1.35e-30	38.09
0-	9.27	-0.84	8.67e-33	10.82
c_8	42.33	-0.96	1.30e-34	11.6
Co	9.3	4.36	8.29e-33	10.69
<i>C</i> 9	37.51	-0.94	1.07e-33	15.23
Can	9.29	3.25	4.74e-33	10.69
c_{10}	36.81	0.09	2.25e-34	12.40
Caa	9.27	-0.67	1.15e-34	10.69
c_{11}	38.51	-0.66	9.17e-37	13.02
Can	9.26	-2.85	3.92e-34	10.69
c_{12}	35.22	-1.93	2.40e-35	12.47
Can	8.65	-0.26	1.21e-26	10.76
c_{13}	29.42	0.10	5.88e-29	14.28
Ct.	10.28	-0.59	2.61e-26	11.21
c_{14}	38.88	-1.93	2.19e-27	14.48
Car	7.32	-3.58	2.04e-27	12.91
c_{15}	33.28	4.25	2.05e-33	16.26

Table 1. Absolute and local minima of the χ^2 (see Eq.(3.1)) for each of the couplings c_j of the effective Hamiltonian (2.1).

range 1 keVee< E'<20 keVee in 0.5 keVee energy bins for a total exposure $\simeq 2.46$ ton year, corresponding to the combination of DAMA/NaI [37], DAMA/LIBRA-phase1 [2, 3] and DAMA/LIBRA-phase2 [20]. In our analysis we will assume constant quenching factors q=0.3 for sodium, 0.09 for iodine and a Gaussian energy resolution $\mathcal{G}(E', E_{ee}) = Gauss(E'|E_{ee},\sigma) = 1/(\sqrt{2\pi}\sigma)exp(-(E'-E_{ee})/2\sigma^2)$ with $\sigma=0.0091$ (E_{ee}/keVee) + 0.448 $\sqrt{E_{ee}}$ /keVee in keVee. To compare the theoretical predictions to the experimental data, for each coupling c_j^p , j=1,3,4...15 we consider 14 energy bins, of 0.5 keVee width, from 1 keVee to 8 keVee, and one high-energy control bin from 8 keVee to 16 keVee ([E_k', E_{k+1}'], k=1,...,15). In particular the combined DAMA phase1-phase2 high-energy spectrum shows a large positive fluctuation in the interval 16 keVee–20 keVee with modulation amplitude $S_m=0.0028\pm0.0006$ cpd/kg/keVee, i.e. a more than 4 σ effect. DAMA does

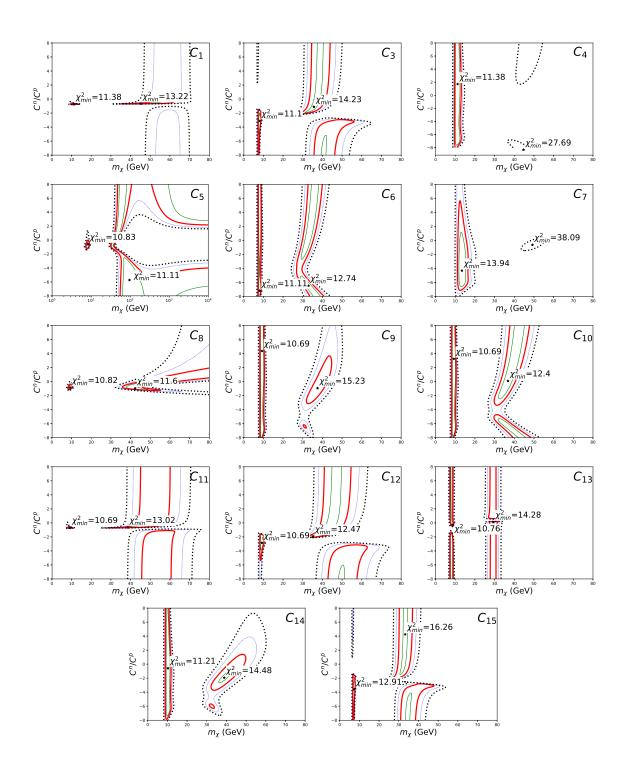


Figure 2. Contour plots of the χ^2 of Eq.(3.1) minimized with respect to σ_p in the m_{χ} -r plane for each of the interaction terms of Eq.(2.1). The thin (green) solid lines, the thick (red) solid lines, the thin (blue) dotted lines, and the thick (black) dotted lines correspond to 2, 3, 4, and 5 σ regions respectively. The best-fit points in the low and high mass regions are shown by the star and the corresponding values of the best-fit parameters are quoted in Table 1.

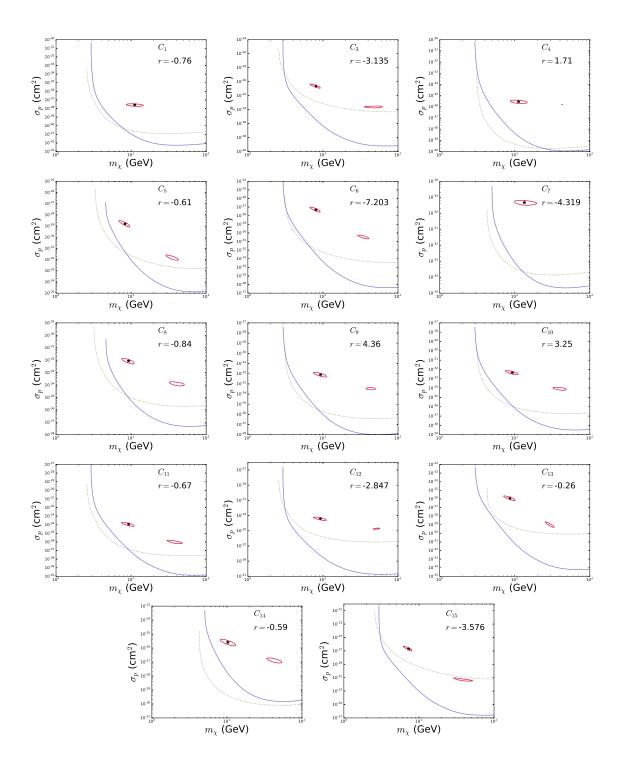


Figure 3. The 5- σ best-fit DAMA regions are compared to the 90% C.L. upper bounds from XENON1T (solid purple line) and PICO60 (green dots) in the m_{χ} - σ_p plane for each of the interaction terms of Eq.(2.1). In each plot the value of r is fixed to the corresponding absolute minima quoted in Table 1 and the star represents the absolute best-fit values of m_{χ} and σ_p .

not provide details about such excess, but the residual rate in the 10 keVee–20 keVee, presumably dominated by the 16 keVee–20 keVee bin, shows random positive and negative fluctuations during the years [20] so it would be questionable to ascribe it to a possible WIMP signal. Moreover, diluting such strong positive fluctuation in a single 8 keVee–20 keVee interval would still yield a 3– σ effect that would bias the fitting procedure without making use of its very peculiar spectral features. For this reason we adopt as a control highenergy bin the interval 8 keVee< E' <16 keVee, where the measured modulation amplitude is $S_m = 0.00040 \pm 0.00046$ cpd/kg/keVee.

We perform our χ^2 test constructing the quantity:

$$\chi^{2}(m_{\chi}, \sigma_{p}, r) = \sum_{k=1}^{15} \frac{\left[S_{m,k} - S_{m,k}^{exp}(m_{\chi}, \sigma_{p}, r) \right]^{2}}{\sigma_{k}^{2}}$$
(3.1)

and minimize it as a function of (m_{χ}, σ_p, r) . In Fig. 1 we show the result of such minimization at fixed WIMP mass m_{χ} . From such figure one can see that for each coupling c_j^p two local minima are obtained. The details of such minima are provided in Table 1. The first thing one can notice from such Table is that all models yield an acceptable χ^2 : in the worst case, i.e. c_7 , $(\chi^2)_{min}=13.94$, with p-value $\simeq 0.30$ with 15-3 degrees of freedom. Moreover, for all of them with the exception of c_7 and c_{15} the absolute minimum of the χ^2 is below or equal to that corresponding the standard SI interaction c_1 .

In addition, the best fit parameters appear to be less tuned compared to the SI case. This can be seen in Fig. 2, where for each of the effective model couplings we provide the contour plots of the χ^2 in the m_{χ} -r plane. In such figures the lines represent contours for $\chi^2 - \chi^2_{min} = n^2$: n=2 for the thin (green) solid lines, n=3 for the thick (red) solid lines, n=4 for the thin (blue) dotted lines and n=5 for the thick (black) dotted lines. In particular, the regions within 2 and 3 σ for c_1 appear strongly tuned to the value r=-0.76, corresponding to a cancellation in the WIMP-iodine cross section, whereas for most of the other effective interactions the corresponding contour encompasses a much wider volume of the parameter space.

In agreement to the analysis of Ref.[31], also the WIMP interpretation of the new DAMA data is in conflict to the constraints from null experiments. To show this in Fig. 3 we compare the best-fit regions in the m_{χ} - σ_p plane to the constraints from XENON1T and PICO60. In each plane the value of the r parameter is fixed to that of the corresponding absolute minimum in Table 1, and the star represents the absolute best-fit values of m_{χ} and σ_p . Moreover, for clarity we only show with a solid (red) closed line the best-fit contour for $\chi^2 - \chi^2_{min} = n^2$ with n=5, while the solid (purple) and dotted (green) open curves represent in each plot the 90% upper bound from XENON1T and PICO60, respectively. From such figure one can conclude that all the best-fit solutions are in tension with the null results of both experiments.

To better understand the impact of the new data (and in particular, the additional two experimental bins below 2 keVee) on the χ^2 in Fig. 4 we show the predicted modulation amplitudes for our best–fit models and compare them to the corresponding experimental data. Moreover, for each effective coupling the contributions from WIMP–sodium (dashes) and WIMP–iodine (dot–dashes) scattering to the total modulation amplitude (solid line) is provided in Fig. 5. In particular, from this latter figure it is evident that, to provide a good fit to the measured modulation amplitudes, a peculiar pattern for the two contributions due to WIMP scattering off sodium and iodine is required, namely a sodium contribution

with maximum at approximately 2 keVee and approaching modulation phase inversion at lower energies, where instead the term due to iodine is steeply increasing. Such behavior is in agreement to the findings of Ref. [25] for the coupling c_1 and holds also for all the other interaction terms of Eq.(2.1). In the case of c_1 the iodine contribution is naturally enhanced compared to that of sodium due to the dependence of the cross section on the square of the atomic mass number of the target (see Eq. (1.1)). As a consequence, the r parameter needs to be tuned to suppress the iodine contribution (i.e. close to the value $r_{Iodine} \simeq -53/(127-53) \simeq -0.7$, see Eq.(1.1)), since below 2 keVee the measured modulation amplitudes are increasing only mildly. In the case of c_1 this inevitably reduces also the sodium contribution, since -Z/(A-Z) is roughly similar (\simeq -0.9) also for sodium, enhancing the fine tuning. This is clearly visible in the first panel of Fig. 2. On the other hand, for all the other interactions of Eq.(2.1) the value of r corresponding to a cancellation in the nuclear response function for iodine is normally unrelated to that for sodium, so that the iodine contribution can be suppressed without reducing that from sodium in a more natural way. On top of that, with the exception of the Φ'' nuclear response function, all the other ones typically show a milder enhancement of the iodine signal compared to that for sodium in the first place. In particular with the exception of c_7 and c_{14} and, to a lesser extent, c_5 and c_{8} , the contribution of the scattering amplitude proportional to $v_T^{\perp 2}$ (see Eq.(A.1) is completely negligible. On the other hand for c_7 and c_{14} only the term proportional to $v_T^{\perp 2}$ is present in the cross section, while for c_5 and c_8 such term is not negligible (for the choice of parameters corresponding to the absolute minima of Table 1 it contributes between 10% and 25% of the modulation amplitude in the first bin due to the iodine contribution through the Mnuclear response function). As a consequence of this, the interaction terms c_4 , c_6 , c_7 , c_9 , c_{10} and c_{14} depend on the spin-dependent nuclear response functions Σ'' and/or Σ' which are proportional, respectively, to the component of the nuclear spin along the direction of the transferred momentum or perpendicular to it. This implies only a factor \simeq two hierarchy between the WIMP-iodine and the WIMP-sodium cross sections. Moreover, in the case of c_5 and c_8 the velocity-independent term of the cross section depends on the Δ response function, which is proportional to the nucleon angular momentum content of the nucleus, favoring elements which have an unpaired nucleon in a non s-shell orbital. Both iodine and sodium have this feature, implying also in this case no large hierarchy between the cross sections off the two nuclei. Namely, numerically the isoscalar response function at vanishing momentum transfer $W_{T\Delta}^{00}(q\to 0)$ for sodium is a factor $\simeq 0.25$ smaller compared to that for iodine. Finally, the WIMP-nucleus cross section for interaction c_{13} is driven by the $\tilde{\Phi}'$ nuclear response function for which $W_{T\tilde{\Phi}'}^{00}(q\to 0)$ for sodium turns out to be a factor $\simeq 6.3$ larger than that for iodine. The bottom line is that, compared to the standard SI interaction, for all such effective models the cross section for scatterings off iodine is naturally less enhanced or even subdominant, implying a lower fine tuning of the parameters. On the other hand, interactions c_3 , c_{12} and c_{15} are driven by the Φ'' nuclear response function, which is sensitive to the product of the nucleon spin and its angular momentum. As a consequence, similarly to the SI case, such interaction favors heavy elements over light ones, leading to a large hierarchy between iodine over sodium. However, as explained above, in this case the value of r corresponding to a suppression of the iodine response function is quite different to that for sodium (for instance, we checked that $r_{iodine} \simeq$ -2.3 and $r_{sodium} \simeq$ -0.7 for a 2 keVee recoil energy). This implies that, at variance with SI scattering, the iodine contribution for Φ'' can be suppressed without reducing that for sodium, and less tuning is needed to obtain a good fit.

We conclude our discussion with a comment about the behavior of the χ^2 at large m_{χ} . As can be seen from Fig. 1 for most models (namely, all those for which the explicit dependence of the cross section from v^{\perp} is negligible) the χ^2 shows a steep rise at large m_{χ} . This can be understood because in this case the predicted modulation amplitude is given by the cosine transform of the rate of Eq. (2.6), which is a function of the v_{min} parameter only, and turns out to be negative for $v_{min} \leq 200 \text{ km/s}$ [25]. Moreover, at fixed recoil energy v_{min} is decreasing with m_{χ} (and eventually independent on it). As a consequence, when m_{χ} is large one has $v_{min} < 200$ km/s in all the energy range of the DAMA signal, implying that the predicted modulation amplitudes result negative. Since the corresponding measured modulation amplitudes are all positive this implies a bad fit to the data and a large χ^2 . Moreover, while in DAMA phase the modulation data showed a maximum with energy, this is no longer true for phase2, where they are monotonically decreasing. This means that, to get an acceptable χ^2 , the contribution to the expected modulation rate of the halo function at small values of $v_{min} \lesssim 300$ km/s must, if present, be subdominant, in order not to lead to a spectrum rising with energy (this requirement is even more stringent in presence of a momentum-dependence of the rate). This means that effects such as gravitational focusing or energy-dependence of the phase [35], which pertain to the $v_{min} \leq 300$ km/s regime of the WIMP velocity distribution integral, can only affect configurations with a large χ^2 . On the other hand, when the cross section shows a non-negligible dependence on v^{\perp} , (i.e. for models c_5 , c_8 , c_7 and c_{14}) the integral of Eq.(2.6) is dominated by large values of v > 200km/s irrespective of v_{min} and positive modulation amplitudes can be obtained in the energy range of the DAMA signal also at large values of m_{χ} , implying in such regime a milder increase of the χ^2 .

4 Conclusions

The DAMA collaboration has released first results from the upgraded DAMA/LIBRA-phase2 experiment [20]. In the present paper we have fitted the updated DAMA result for the modulation amplitudes in terms of a WIMP signal, parameterizing the WIMP-nucleus interaction in terms of the most general WIMP-nucleus effective Lagrangian for a WIMP particle of spin 0 or spin 1/2. In particular we have systematically assumed the dominance of one of the 14 possible interaction terms of the Hamiltonian of Eq. (2.1) and fitted the experimental amplitudes to the three parameters m_{χ} (WIMP mass), σ_p (WIMP-nucleon effective cross-section) and c^n/c^p (neutron over proton coupling) assuming for the WIMP velocity distribution a standard Maxwellian. Our results show that with only the two exceptions of c_7 and c_{15} all the couplings of the non-relativistic effective Hamiltonian can provide a better fit compared to the SI case (see Table 1), and with a reduced fine-tuning of the parameters (see Fig. 2). This is explained by the fact that in the new DAMA data the energy threshold has been lowered from 2 keVee to 1 keVee, and the new energy bins are sensitive to WIMP-iodine scatterings also for a low WIMP mass. In the SI case this requires to highly tune the parameters to suppress the iodine contribution, in order to avoid an otherwise too steeply increasing spectrum at low energy of the modulation amplitudes compared to the data. On the other hand, if the WIMP-nucleus cross section is driven by other operators the fine tuning required to suppress iodine is reduced and/or the hierarchy between the WIMP-iodine and the WIMP-sodium cross section is less pronounced in the first place. Moreover, we have observed that effective models for which the cross section depends explicitly on the WIMP incoming velocity show a different phase of the modulation amplitudes at large values of the

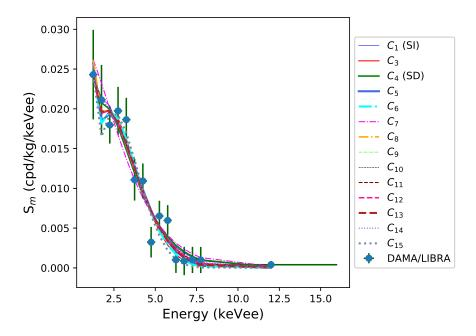


Figure 4. DAMA modulation amplitudes as a function of the measured ionization energy E_{ee} for the absolute minima of each effective model. The points with error bars correspond to the combined data of DAMA/NaI [37], DAMA/LIBRA-phase1 [2, 3] and DAMA/LIBRA-phase2 [20].

WIMP mass compared to the standard velocity–independent cross–section, allowing to get a better fit of the DAMA data. As shown in Fig. 3 all the best fit solutions are in tension with exclusion plots of both XENON1T and PICO60.

Acknowledgments

This research was supported by the Basic Science Research Program through the National Research Foundation of Korea(NRF) funded by the Ministry of Education, grant number 2016R1D1A1A09917964.

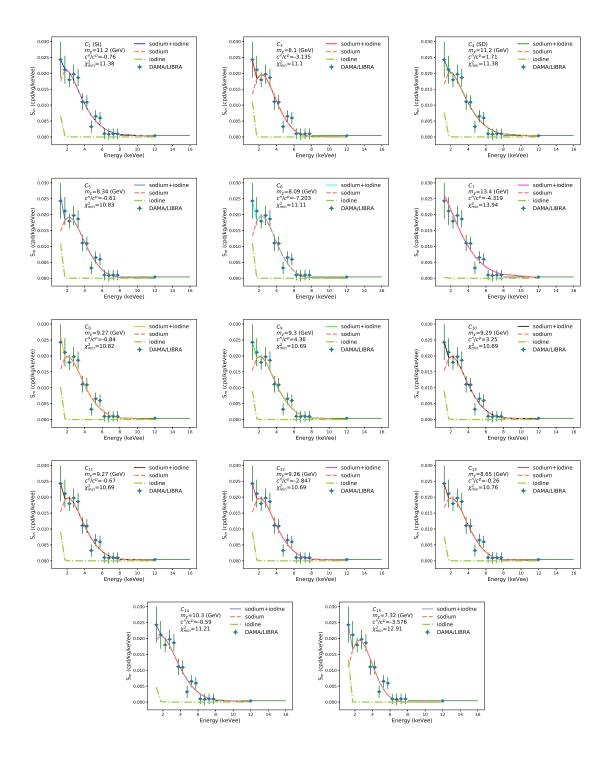


Figure 5. DAMA modulation amplitudes as a function of the ionization energy E_{ee} for the absolute minimum of each of the interaction terms of Eq.(2.1). The DAMA data points with corresponding error bars are shown in green color. The salmon (dashed) and yellowgreen (dot-dashed) lines show the contributions to the modulation amplitude from WIMP scattering off sodium and iodine respectively. The combined contributions (sodium+iodine) of each model are shown by a solid line.

A WIMP response functions

We collect here the WIMP particle-physics response functions introduced in Eq.(2.5) and adapted from [29, 30]:

$$\begin{split} R_{M}^{\tau\tau'}\left(v_{T}^{+2},\frac{q^{2}}{m_{N}^{2}}\right) &= c_{1}^{\tau}c_{1}^{\tau'} + \frac{j_{\chi}(j_{\chi}+1)}{3} \left[\frac{q^{2}}{m_{N}^{2}}v_{T}^{+2}c_{5}^{\tau}c_{5}^{\tau'} + v_{T}^{+2}c_{8}^{\tau}c_{8}^{\tau'} + \frac{q^{2}}{m_{N}^{2}}c_{11}^{\tau}c_{11}^{\tau'}\right] \\ R_{\Phi''}^{\tau\tau'}\left(v_{T}^{+2},\frac{q^{2}}{m_{N}^{2}}\right) &= \left[\frac{q^{2}}{4m_{N}^{2}}c_{3}^{\tau}c_{3}^{\tau'} + \frac{j_{\chi}(j_{\chi}+1)}{12}\left(c_{12}^{\tau} - \frac{q^{2}}{m_{N}^{2}}c_{15}^{\tau}\right)\left(c_{12}^{\tau} - \frac{q^{2}}{m_{N}^{2}}c_{15}^{\tau}\right)\right] \frac{q^{2}}{m_{N}^{2}} \\ R_{\Phi''M}^{\tau\tau'}\left(v_{T}^{+2},\frac{q^{2}}{m_{N}^{2}}\right) &= \left[c_{3}^{\tau}c_{1}^{\tau'} + \frac{j_{\chi}(j_{\chi}+1)}{3}\left(c_{12}^{\tau}c_{12}^{\tau'} + \frac{q^{2}}{m_{N}^{2}}c_{15}^{\tau}\right)c_{11}^{\tau'}\right] \frac{q^{2}}{m_{N}^{2}} \\ R_{\Phi''M}^{\tau\tau'}\left(v_{T}^{+2},\frac{q^{2}}{m_{N}^{2}}\right) &= \left[\frac{j_{\chi}(j_{\chi}+1)}{12}\left(c_{12}^{\tau}c_{12}^{\tau'} + \frac{q^{2}}{m_{N}^{2}}c_{13}^{\tau}c_{13}^{\tau'}\right)\right] \frac{q^{2}}{m_{N}^{2}} \\ R_{\Sigma''}^{\tau\tau'}\left(v_{T}^{+2},\frac{q^{2}}{m_{N}^{2}}\right) &= \frac{q^{2}}{4m_{N}^{2}}c_{10}^{\tau}c_{10}^{\tau'} + \frac{j_{\chi}(j_{\chi}+1)}{12}\left[c_{4}^{\tau}c_{1}^{\tau'} + \frac{q^{2}}{m_{N}^{2}}c_{13}^{\tau'}c_{13}^{\tau'}\right] \\ R_{\Sigma''}^{\tau\tau'}\left(v_{T}^{+2},\frac{q^{2}}{m_{N}^{2}}\right) &= \frac{1}{8}\left[\frac{q^{2}}{m_{N}^{2}}v_{T}^{+2}c_{3}^{\tau}c_{3}^{\tau'} + v_{T}^{+2}c_{7}^{\tau}c_{7}^{\tau'}\right] + \frac{j_{\chi}(j_{\chi}+1)}{12}\left[c_{4}^{\tau}c_{4}^{\tau'} + \frac{q^{2}}{m_{N}^{2}}v_{T}^{+2}c_{13}^{\tau}c_{13}^{\tau'}\right] \\ R_{\Delta}^{\tau\tau'}\left(v_{T}^{+2},\frac{q^{2}}{m_{N}^{2}}\right) &= \frac{j_{\chi}(j_{\chi}+1)}{3}\left(\frac{q^{2}}{m_{N}^{2}}c_{5}^{\tau}c_{5}^{\tau'} + c_{8}^{\tau}c_{8}^{\tau'}\right)\frac{q^{2}}{m_{N}^{2}} \\ R_{\Delta}^{\tau\tau'}\left(v_{T}^{+2},\frac{q^{2}}{m_{N}^{2}}\right) &= \frac{j_{\chi}(j_{\chi}+1)}{3}\left(c_{5}^{\tau}c_{4}^{\tau'} - c_{8}^{\tau}c_{9}^{\tau'}\right)\frac{q^{2}}{m_{N}^{2}}. \end{split}$$

$$(A.1)$$

B Constraints

In the present analysis we include the constraints from XENON1T [5] and PICO60 [19].

B.1 XENON1T

For XENON1T we have assumed zero WIMP candidate events in the range 3 PE $\leq S_1 \leq$ 30 PE in the lower half of the signal band, as shown in figure 2 of Ref.[5] for the primary scintillation signal S1 (directly in Photo Electrons, PE) for an exposure of 34.2 days and a fiducial volume of 1042 kg of xenon. We have used the efficiency taken from Fig. 1 of [5], a light collection efficiency g_1 =0.144, while for the light yield L_y we have used the NEST model of Ref. [38] with an electric field E=120 V/cm and the parameters of Table 1 with the exception of the Lindhard parameter k=0.15, to reproduce the combined energy curves of Fig. 2b of [5].

For XENON1T we have modeled the energy resolution combining a Poisson fluctuation of the observed primary signal S_1 compared to $\langle S_1 \rangle$ and a Gaussian response of the photomultiplier with $\sigma_{PMT} = 0.5$, so that:

$$\mathcal{G}_{Xe}(E_R, S) = \sum_{n=1}^{\infty} Gauss(S|n, \sqrt{n}\sigma_{PMT})Poiss(n, \langle S(E_R) \rangle),$$
 (B.1)

with $Poiss(n, \lambda) = \lambda^n/n!exp(-\lambda)$.

B.2 PICO60

PICO60 [19] uses C_3F_8 as the target. Only the threshold E_{th} =3.3 keV was analyzed, with a total exposure of 1167.0 kg day and 0 event detected. We use for fluorine and carbon the nucleation probabilities of Fig. 4 of [18].

References

- [1] Planck Collaboration, P. A. R. Ade et al., Planck 2013 results. XVI. Cosmological parameters, Astron. Astrophys. 571 (2014) A16, [arXiv:1303.5076].
- [2] **DAMA** Collaboration, R. Bernabei et al., First results from DAMA/LIBRA and the combined results with DAMA/NaI, Eur. Phys. J. C56 (2008) 333–355, [arXiv:0804.2741].
- [3] **DAMA**, **LIBRA** Collaboration, R. Bernabei et al., New results from DAMA/LIBRA, Eur. Phys. J. **C67** (2010) 39–49, [arXiv:1002.1028].
- [4] R. Bernabei et al., Final model independent result of DAMA/LIBRA-phase1, Eur. Phys. J. C73 (2013) 2648, [arXiv:1308.5109].
- [5] **XENON** Collaboration, E. Aprile et al., First Dark Matter Search Results from the XENON1T Experiment, Phys. Rev. Lett. 119 (2017), no. 18 181301, [arXiv:1705.06655].
- [6] LUX Collaboration, D. S. Akerib et al., First results from the LUX dark matter experiment at the Sanford Underground Research Facility, Phys. Rev. Lett. 112 (2014) 091303, [arXiv:1310.8214].
- [7] **XENON100** Collaboration, E. Aprile et al., Dark Matter Results from 225 Live Days of XENON100 Data, Phys. Rev. Lett. 109 (2012) 181301, [arXiv:1207.5988].
- [8] XENON10 Collaboration, J. Angle et al., A search for light dark matter in XENON10 data, Phys. Rev. Lett. 107 (2011) 051301, [arXiv:1104.3088]. [Erratum: Phys. Rev. Lett.110,249901(2013)].
- [9] S. C. Kim et al., New Limits on Interactions between Weakly Interacting Massive Particles and Nucleons Obtained with CsI(Tl) Crystal Detectors, Phys. Rev. Lett. 108 (2012) 181301, [arXiv:1204.2646].
- [10] Y. Kim, Recent progress in KIMS experiment, talk given at 13th International Conference on Topics in Astroparticle and Underground Physics, September 8–13 2013, Asilomar, California USA (TAUP2013).
- [11] CDMS-II Collaboration, Z. Ahmed et al., Results from a Low-Energy Analysis of the CDMS II Germanium Data, Phys. Rev. Lett. 106 (2011) 131302, [arXiv:1011.2482].
- [12] SuperCDMS Collaboration, R. Agnese et al., Search for Low-Mass Weakly Interacting Massive Particles Using Voltage-Assisted Calorimetric Ionization Detection in the SuperCDMS Experiment, Phys. Rev. Lett. 112 (2014), no. 4 041302, [arXiv:1309.3259].
- [13] SuperCDMS Collaboration, R. Agnese et al., Search for Low-Mass Weakly Interacting Massive Particles with SuperCDMS, Phys. Rev. Lett. 112 (2014), no. 24 241302, [arXiv:1402.7137].
- [14] SuperCDMS Collaboration, R. Agnese et al., Improved WIMP-search reach of the CDMS II germanium data, Phys. Rev. D92 (2015), no. 7 072003, [arXiv:1504.05871].
- [15] M. Felizardo et al., Final Analysis and Results of the Phase II SIMPLE Dark Matter Search, Phys. Rev. Lett. 108 (2012) 201302, [arXiv:1106.3014].

- [16] COUPP Collaboration, E. Behnke et al., First Dark Matter Search Results from a 4-kg CF₃I Bubble Chamber Operated in a Deep Underground Site, Phys. Rev. **D86** (2012), no. 5 052001, [arXiv:1204.3094]. [Erratum: Phys. Rev.D90,no.7,079902(2014)].
- [17] **PICASSO** Collaboration, S. Archambault et al., Constraints on Low-Mass WIMP Interactions on ¹⁹F from PICASSO, Phys. Lett. **B711** (2012) 153–161, [arXiv:1202.1240].
- [18] **PICO** Collaboration, C. Amole et al., Dark Matter Search Results from the PICO-2L C₃F₈ Bubble Chamber, Phys. Rev. Lett. 114 (2015), no. 23 231302, [arXiv:1503.00008].
- [19] **PICO** Collaboration, C. Amole et al., Dark Matter Search Results from the PICO-60 C₃F₈ Bubble Chamber, Phys. Rev. Lett. 118 (2017), no. 25 251301, [arXiv:1702.07666].
- [20] R. Bernabei et al., First model independent results from DAMA/LIBRA-phase2, arXiv:1805.10486.
- [21] C. Kelso, C. Savage, M. Valluri, K. Freese, G. S. Stinson, and J. Bailin, *The impact of baryons on the direct detection of dark matter*, *JCAP* **1608** (2016) 071, [arXiv:1601.04725].
- [22] A. M. Green, Astrophysical uncertainties on direct detection experiments, Mod. Phys. Lett. A27 (2012) 1230004, [arXiv:1112.0524].
- [23] A. Bottino, F. Donato, N. Fornengo, and S. Scopel, Lower bound on the neutralino mass from new data on CMB and implications for relic neutralinos, Phys. Rev. **D68** (2003) 043506, [hep-ph/0304080].
- [24] A. Bottino, F. Donato, N. Fornengo, and S. Scopel, Light neutralinos and WIMP direct searches, Phys. Rev. D69 (2004) 037302, [hep-ph/0307303].
- [25] S. Baum, K. Freese, and C. Kelso, Dark Matter implications of DAMA/LIBRA-phase2 results, arXiv:1804.01231.
- [26] F. Kahlhoefer, F. Reindl, K. Schffner, K. Schmidt-Hoberg, and S. Wild, Model-independent comparison of annual modulation and total rate with direct detection experiments, arXiv:1802.10175.
- [27] B. A. Dobrescu and I. Mocioiu, Spin-dependent macroscopic forces from new particle exchange, JHEP 11 (2006) 005, [hep-ph/0605342].
- [28] J. Fan, M. Reece, and L.-T. Wang, Non-relativistic effective theory of dark matter direct detection, JCAP 1011 (2010) 042, [arXiv:1008.1591].
- [29] A. L. Fitzpatrick, W. Haxton, E. Katz, N. Lubbers, and Y. Xu, The Effective Field Theory of Dark Matter Direct Detection, JCAP 1302 (2013) 004, [arXiv:1203.3542].
- [30] N. Anand, A. L. Fitzpatrick, and W. C. Haxton, Weakly interacting massive particle-nucleus elastic scattering response, Phys. Rev. C89 (2014), no. 6 065501, [arXiv:1308.6288].
- [31] R. Catena, A. Ibarra, and S. Wild, DAMA confronts null searches in the effective theory of dark matter-nucleon interactions, JCAP 1605 (2016), no. 05 039, [arXiv:1602.04074].
- [32] R. Catena and B. Schwabe, Form factors for dark matter capture by the Sun in effective theories, JCAP 1504 (2015), no. 04 042, [arXiv:1501.03729].
- [33] S. E. Koposov, H.-W. Rix, and D. W. Hogg, Constraining the Milky Way potential with a 6-D phase-space map of the GD-1 stellar stream, Astrophys. J. **712** (2010) 260–273, [arXiv:0907.1085].
- [34] T. Piffl et al., The RAVE survey: the Galactic escape speed and the mass of the Milky Way, Astron. Astrophys. 562 (2014) A91, [arXiv:1309.4293].
- [35] S. K. Lee, M. Lisanti, A. H. G. Peter, and B. R. Safdi, Effect of Gravitational Focusing on Annual Modulation in Dark-Matter Direct-Detection Experiments, Phys. Rev. Lett. 112 (2014), no. 1 011301, [arXiv:1308.1953].

- [36] K. Freese, M. Lisanti, and C. Savage, Colloquium: Annual modulation of dark matter, Rev. Mod. Phys. 85 (2013) 1561–1581, [arXiv:1209.3339].
- [37] R. Bernabei et al., Searching for WIMPs by the annual modulation signature, Phys. Lett. **B424** (1998) 195–201.
- [38] B. Lenardo, K. Kazkaz, A. Manalaysay, J. Mock, M. Szydagis, and M. Tripathi, A Global Analysis of Light and Charge Yields in Liquid Xenon, IEEE Trans. Nucl. Sci. 62 (2015), no. 6 3387–3396, [arXiv:1412.4417].